Anomalous Diffusion of Fast Ions in the Presence of Fishbone Instabilities in Tokamaks

Master's Thesis in Physics

September 2008 - January 2009

Alexandre Bovet

Supervisor
Dr Simon Pinches (Culham, UKAEA)

Responsible Professor
Prof. Ambrogio Fasoli (CRPP, EPFL)

EIDGENÖSSISCHE TECHNISCHE HOCHSCHULE LAUSANNE
POLITECNICO FEDERALE DI LOSANNA
SWISS FEDERAL INSTITUTE OF TECHNOLOGY LAUSANNE

CENTRE DE RECHERCHES EN PHYSIQUE DES PLASMAS
Association EURATOM - Confédération Suisse
Bat. PPB - Station 13
CH - 1015 LAUSANNE
TELEPHONE: +41 21 - 693 34 87 TELEFAX: +41 21 - 693 51 76

ÉCOLE POLYTECHNIQUE
FÉDÉRALE DE LAUSANNE

Travail pratique de Master en Physique

Session de septembre 2008 - février 2009

Candidat : Alexandre BOVET

Anomalous diffusion of fast ions in the presence of fishbone instabilities in tokamaks

Aim:

To investigate whether the anomalous fast ion diffusion [$D \sim 0.5 m^2/s$] needed to explain the observed NBI driven current profile, can be explained by fast ion re-distribution caused by fishbone modes.

Plan:

- Set up simulation of MAST #18808
  - Learn how to look at experimental data / MHD present in plasma using Specview & XPAD *(Simon Pinches)*
  - Generate equilibrium using EFIT++ / HELENA *(Lynton Appel)*
  - Obtain linear eigenfunction of fishbone modes ($n = 1$ internal kink)
    - Stability calculation with MISHKA / CASTOR *(Ian Chapman / Samuli Saarelma)*
    - Check consistency with experimental SXR observations *(Minh-Duc Hua)*
  - Specify fast ion distribution
    - Obtain from TRANSP simulation *(Mikhail Turnianski)*
  - Compile HAGIS code for COLUMBUS parallel computer *(Terry Martin)*
- Run simulation
- Interpret results
  - Model changes in fast ion distribution as diffusion + pinch
- Compare with transport simulations of experimental data (TRANSP)

The work shall be supervised by Dr. Simon Pinches at Culham, UKAEA.

The candidate will submit 5 typed reports of his report.

Lausanne, 23 September 2008 Prof. A. Fasoli

Contents

1 Introduction

Fast ions, whether produced by fusion reactions, or by ionisation of neutral beam, are expected to play a major role in the heating of burning plasmas. Therefore, the study of the fast ion's behaviour in tokamaks is important for the future burning plasma experiments such as ITER.

Understanding the effect of neutral beam injection on the current profile is also important for current profile control and for achieving steady state scenarios where non-inductive current drive is necessary.

Several plasma discharges have been carried out in the MAST tokamak to investigate to which extent the q-profile may be modified by neutral beam current drive (NBCD) [1]. TRANSP simulations of the beam deposition [2] during steady state experiments, with off-axis NBCD, have been carried out. It has been found that an anomalous diffusion (with a diffusion coefficient of roughly $D_b \sim 0.5\,\mathrm{m}^2/\mathrm{s}$) of the fast ion is needed to explain the significantly lower neutron rate measured than predicted by the TRANSP code using an assumption of classical beam deposition and collisional thermalisation. TRANSP simulations show that this diffusion broadens the fast ion deposition profile and may help to avoid harmful instabilities [1]. This anomalous diffusion is suspected to be caused by fishbone instabilities, as the time of the largest discrepancy between simulated and measured neutron rates correlates well with the highest magnitude of fishbone activity.

The aim of this work is to investigate, with simulations of the HAGIS code [3], if the interaction between fast ion resulting from off-axis NBCD and fishbone instabilities may be responsible for the fast ion anomalous diffusion needed to explain the observed neutron rate.

2 MAST Device

The Mega Ampere Spherical Tokamak (MAST) is a tight aspect ratio tokamak in operation at Culham Science Centre since 2000 (Table. 1). It is the successor of START (Small Tight Aspect Ratio Tokamak) which achieved record beta values of around 40% [4]. The cross section and the plasma current of MAST is comparable to those of conventional aspect ratio tokamaks such as DIII-D and ASDEX Upgrade.

The Mega Ampere Spherical Tokamak	
Major radius, R (m)	0.85
Minor radius, a (m)	0.65
Elongation, κ	1.6-2.5
Aspect ratio, R/a	≥ 1.3
Plasma current, I_p (MA)	< 1.5
Toroidal field, B_t (T)	≤ 0.62
NBI heating power, P_{NBI} (MW)	5

Table 1 – Key parameters for MAST
[1, 4]

As the plasma current in tokamaks scales with the inverse aspect ratio ($I_p \sim (aB_t/q)/(R/a)$), the advantage of spherical tokamaks (with small aspect ratio, R/a) is that, for a given plasma current I_p, a smaller toroidal field is required to achieve the same safety factor q than with conventional tokamaks. Thus, high plasma currents are more easily achieved in spherical tokamaks and they are convenient to test physics models under extreme conditions.

The main heating in MAST is provided by two mid-plane co-injected deuterium neutral beam with a total power up to 5 MW. The injected beams have energies up to 70 keV and a tangency radius of 0.7 m and lead to a driven current contribution up to ∼40 % [1].

3 Theoretical Review

3.1 Transport in Magnetically Confined Plasmas

Determining the quality of the confinement of devices such as tokamaks, transport study is of main importance. Two types of transport are distinguished : classical (and neoclassical) and anomalous transport.

3.1.1 Classical and Neoclassical Transport

The classical transport of energy and thermal particles across a homogeneous magnetic field is due to Coulomb collisions. It can be seen as a random walk with a step length of the electron Larmor radius, ρ_e and frequency of the electron-ion collision frequency, $1/\tau_e$ [5], for which the diffusion coefficient is given by

$$D_{classical} \sim \frac{\rho_e^2}{\tau_e} \sim 1.789 \times 10^{-23} \frac{n}{T_e^{1/2} B^2} \, [\mathrm{m}^2/\mathrm{s}] \, ,$$

where the electron temperature is in keV, the density is in m^{-3} and the magnetic field in Tesla. For a typical MAST plasma with $n = 3 \times 10^{19}$ m^{-3}, $B = 0.53$ T and $T_e = 1.5$ keV, the classical diffusion coefficient for thermal particles is $D_{classical} \sim 1.56 \times 10^{-3}$ m^2/s.

The neoclassical transport is also based on the Coulomb collisions but takes into account the toroidal geometry of a tokamak. The effect of trapped particles, having banana orbits, and convection due to the $\boldsymbol{\nabla B}$ drift and the $\boldsymbol{E} \times \boldsymbol{B}$ drift is to increase the value of the diffusivity which, now, depends on the collisionality.

For low collisionality, the trapped particles dominate the transport. An approximate expression for the diffusion coefficient can be derived considering a random walk with a step length of the banana orbit's width and taking into account only the fraction of trapped particles. The banana orbit's width being bigger than the Larmor radius, the found diffusion coefficient is bigger than the classical (by $q^2/\epsilon^{3/2}$, where q is the safety factor and ϵ is the inverse aspect-ratio). An accurate calculation of this coefficient can be made starting from the kinetic equation.

When the collisionality is high, Pfirsch-Schluter diffusion, which takes the additional flux due to toridicity into consideration, dominates and gives

a diffusion coefficient exceeding the classical one by $2q^2\eta_\parallel/\eta_\perp$, which is about an order of magnitude greater [5].

3.1.2 Anomalous Transport

The measured experimental confinement times are regrettably much shorter than the predicted ones with the neoclassical diffusion coefficient and don't even scale with the same parameters [4]. It indicates that the main process governing transport in tokamak's plasmas is not the Coulomb collisions.

It has been found that it is rather the transport resulting from the fluctuating electric and magnetic fields, known as anomalous transport. In tokamaks, a variety of waves can propagate in the plasma and become instable, growing by extracting its energy. The free energy released by instabilities leads to the establishment of an equilibrium fluctuation of the perturbed quantities. The resulting fluctuating $\boldsymbol{E} \times \boldsymbol{B}$ drift velocity transports particles and energy radially.

The theoretical study of the associated transport requires an elaborate nonlinear analysis and diffusion coefficient are often estimated experimentally or numerically.

3.2 Instabilities

The first approach to study instabilities in magnetic plasmas is to begin with the magnetohydrodynamic equations describing an equilibrium state and to linearise them around this equilibrium in order to determine whether it is stable or unstable to arbitrarily small perturbations. This analysis is usually carried out using a variational form of the equations, called the energy principle.

3.2.1 Ideal MHD equations

The ideal MHD model describes a perfectly conducting fluid in magnetic and electric fields. The ideal MHD equations are [6]

$$\rho\frac{d\boldsymbol{v}}{dt} = \rho(\frac{\partial \boldsymbol{v}}{\partial t} + \boldsymbol{v}\cdot\boldsymbol{\nabla}) = -\boldsymbol{\nabla}p + \boldsymbol{J}\times\boldsymbol{B}\ , \tag{1}$$

$$\boldsymbol{J} = \frac{1}{\mu}\boldsymbol{\nabla}\times\boldsymbol{B}\ , \tag{2}$$

$$\frac{\partial \boldsymbol{B}}{\partial t} = -\boldsymbol{\nabla}\times\boldsymbol{E}\ , \tag{3}$$

$$\boldsymbol{E} = -\boldsymbol{v}\times\boldsymbol{B}\ , \tag{4}$$

$$\frac{\partial p}{\partial t} = -\boldsymbol{v}\cdot\boldsymbol{\nabla}p - \Gamma p\boldsymbol{\nabla}\cdot\boldsymbol{v}\ , \tag{5}$$

$$\frac{\partial \rho}{\partial t} = -\boldsymbol{v}\cdot\boldsymbol{\nabla}\rho - \rho\boldsymbol{\nabla}\cdot\boldsymbol{v}\ , \tag{6}$$

where $\boldsymbol{v}$ is the macroscopic fluid velocity, $\boldsymbol{J}$ is the current density, $\boldsymbol{B}$ is the magnetic field, $\boldsymbol{E}$ is the electric field, p is the pressure, ρ is the mass density and $\Gamma = 5/3$ is the ratio of specific heats for an ideal gas with three degrees of freedom.

In this model, ions and electrons are included in one fluid. This assumption is valid only if the relevant time scale, τ is longer than the longest time scale of the two species, namely the ions. Therefore we must have $\tau \gg \Omega_i^{-1}$ where Ω_i is the ion cyclotron frequency. As the gyro-motion of the particles is neglected, the relevant space scale must be larger than the largest length scale of the two species, the ion Larmor radius, $L \gg \rho_i$.

3.2.2 Linearised Equations

The next step in studying perturbations is to linearise the ideal MHD equations by considering an arbitrarily small perturbation from a stationary equilibrium with no flow ($\boldsymbol{v} = 0$), scalar pressure, and no body forces such as gravity or neutral gas pressure [6], leading to

$$
\begin{aligned}
\rho^0 \frac{\partial \boldsymbol{v}^1}{\partial t} &= -\boldsymbol{\nabla} p^1 + \boldsymbol{J}^0 \times \boldsymbol{B}^1 + \boldsymbol{J}^1 \times \boldsymbol{B}^0 \ , && (7)\\
\boldsymbol{J}^1 &= \frac{1}{\mu} \boldsymbol{\nabla} \times \boldsymbol{B}^1 \ , && (8)\\
\frac{\partial \boldsymbol{B}^1}{\partial t} &= \boldsymbol{\nabla} \times (\boldsymbol{v}^1 \times \boldsymbol{B}^0) \ , && (9)\\
\frac{\partial p^1}{\partial t} &= -\boldsymbol{v}^1 \cdot \boldsymbol{\nabla} p^0 - \Gamma p^0 \boldsymbol{\nabla} \cdot \boldsymbol{v}^1 \ , && (10)
\end{aligned}
$$

where the superscript 0 denotes the equilibrium quantities and the superscript 1 denotes the perturbed quantities. The equation for the perturbed density is not needed because it doesn't appear in the other equations.

By integrating equations (9) and (10) and writing them in terms of the displacement vector $\boldsymbol{\xi}(\boldsymbol{x}, t) \equiv \int_0^t dt' \boldsymbol{v}^1(\boldsymbol{x}, t')$ we can combine the linearised equations into a single second order partial differential equation for the displacement vector

$$
\begin{aligned}
\rho^0 \frac{\partial^2 \boldsymbol{\xi}}{\partial t^2} &= \boldsymbol{F}\{\boldsymbol{\xi}\} \ , && (11)\\
&= \boldsymbol{\nabla}(\boldsymbol{\xi} \cdot \boldsymbol{\nabla} p^0 + \Gamma p^0 \boldsymbol{\nabla} \cdot \boldsymbol{\xi})\\
&\quad + \frac{1}{\mu} (\boldsymbol{\nabla} \times \boldsymbol{B^0}) \times \left[\boldsymbol{\nabla} \times (\boldsymbol{\xi} \times \boldsymbol{B}^0)\right]\\
&\quad + \frac{1}{\mu} (\boldsymbol{\nabla} \times \left[\boldsymbol{\nabla} \times (\boldsymbol{\xi} \times \boldsymbol{B}^0)\right]) \times \boldsymbol{B}^0 \ ,
\end{aligned}
$$

where $\boldsymbol{F}\{\boldsymbol{\xi}\}$ is called the force-operator.

3.2.3 Energy Principle

The energy principle is derived by multiplying equation (11) by the time derivative of the displacement vector and integrating over the volume of the plasma. Using the self-adjointness of the force-operator [6], one can finally find the energy principle

$$
\frac{\partial}{\partial t} \left[\underbrace{\int d^3x \frac{1}{2} \rho^0 \dot{\boldsymbol{\xi}}^2}_{\text{kinetic energy}} \underbrace{- \frac{1}{2} \int d^3x \boldsymbol{\xi} \cdot \boldsymbol{F}\{\boldsymbol{\xi}\}}_{\text{potential energy}} \right] = 0 \ , \qquad (12)
$$

indicating that the total perturbed energy is constant in time. Therefore, any perturbation decreasing the potential energy produces a corresponding increase in the kinetic energy which indicates that the system is linearly unstable. On the other hand, if all perturbations lead to an increase in the potential energy, then the system is linearly stable to exponentially growing modes.

The first manner of classifying instabilities is with regards to their sensitivity to boundary conditions. When their existence doesn't depend on the presence of a vacuum layer between the plasma and the wall, they are called internal instabilities. Otherwise, they are called external instabilities.

Generally, to study instabilities in a tokamak, a Fourier decomposition in the toroidal geometry is used

$$\xi(r,\theta,\phi) = \sum_{m,n} \xi_{m,n}(r) e^{i(n\phi - m\theta - \omega t)} \tag{13}$$

where m is the poloidal mode number and n is the toroidal mode number. This transformation allows to study the problem as an eigenvalue problem.

3.2.4 Fishbone Instability

The fishbone instability often occurs when a high energy neutral beam injection (NBI) system is used to heat the plasma and can lead to significant losses of the NBI-produced energetic ions, thus reducing the efficiency of plasma heating [7]. It is characterised by repetitive bursts (fig. 1) with the mode frequency decreasing during each burst (fig. 2).

One distinguishes two branches of the fishbone mode [8]. The high-frequency "precessional branch" results from the interaction between the energetic trapped particles and the $m = 1$, $n = 1$ internal kink mode (fig. 3). The toroidal wave velocity of the instability resonates with the toroidal drift of the trapped particles.

The low-frequency branch is the "diamagnetic branch" and arises from the oscillation of the $m = 1$, $n = 1$ internal kink mode with the bulk ion diamagnetic frequency, ω_{*i} [9]. In this case, the source of energy for the instability is related to the pressure gradient of the plasma bulk [10].

Concerning the precessional fishbone mode, a dispersion relation can be derived from the energy principle assuming a fixed conducting boundary

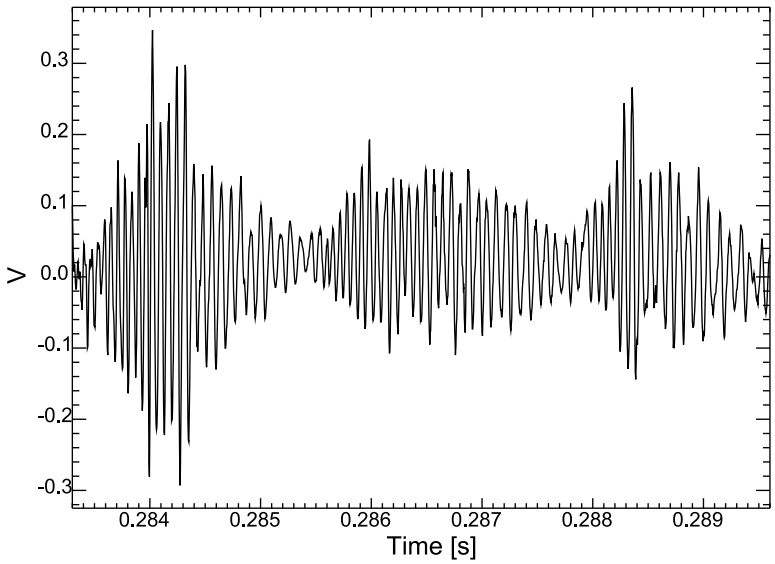

Figure 1 – Mirnov coil's trace of a fishbone instability during MAST shot 18808. One can easily figure out from where comes the instability's name

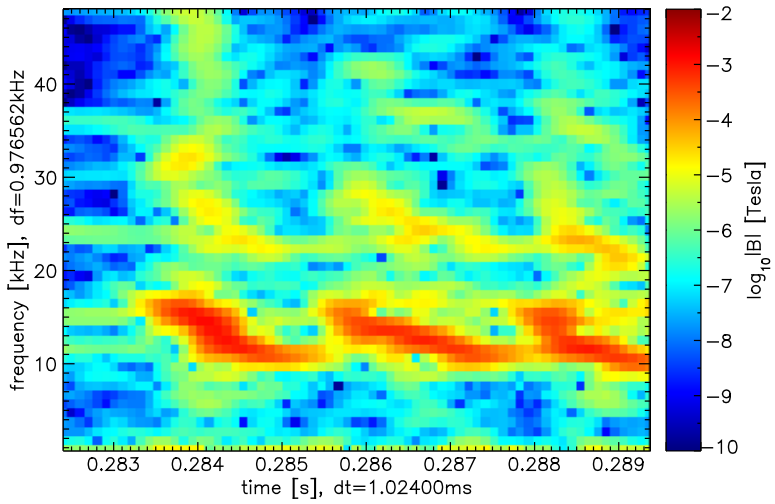

Figure 2 – Mirnov coil's RMS values spectrum during MAST shot 18808 showing the decreasing of the mode frequency by about a factor of two.

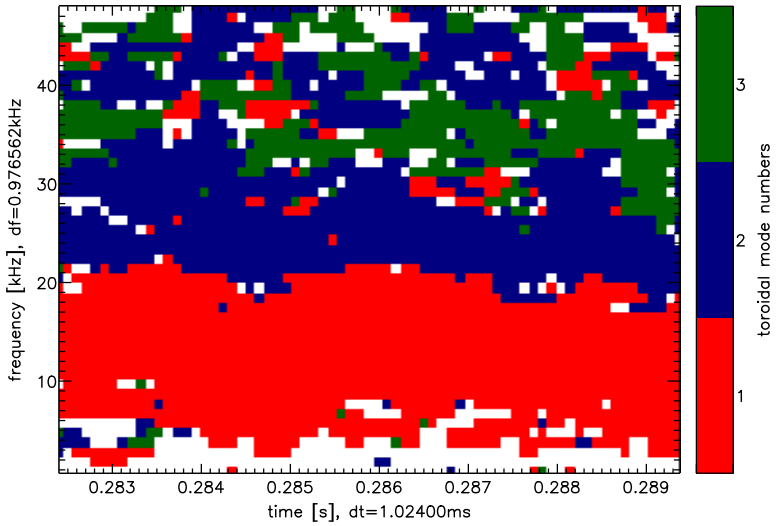

Figure 3 – Mirnov coil's mode number analysis during MAST shot 18808 showing that the mode has a toroidal mode number equal to one.

[11, 4], giving

$$-\frac{i\omega}{\omega_A} + \delta\tilde{W}_p + \omega \int \frac{\phi(\omega, \boldsymbol{v}, r)}{\omega_d - \omega} \frac{\partial f_h}{\partial r} d^3v d^3r = 0$$

where $\omega_A = (B_\phi/R)/(\mu_0\rho)^{1/2}$ is the Alfven frequency, ω_d is the toroidal precession frequency of the trapped particles, and $\delta\tilde{W}_p$ is the normalised MHD potential energy change in the plasma. The first two terms represent the ideal MHD results for the $m = 1$ internal kink and the last term is the trapped fast particles contribution introducing a resonance at $\omega = \omega_d$. The $\frac{\partial f_h}{\partial r}$ term indicates that the instability is driven by the radial gradient in the fast particle distribution function f_h.

4 Fast Particles Modelling

The code used to simulate the interaction between the fast ions and the electromagnetic perturbation is HAGIS (HAmiltonian GuIding centre System) [3]. This code follows the fast ions with a guiding centre Hamiltonian description in straight magnetic field line coordinates (Boozer coordinates) and describes the electromagnetic field as an axisymetric equilibrium field plus a spectrum of instabilities. It uses a 4th order adaptive step size Runge-Kutta method to simultaneously evolve the fast ion distribution and the electromagnetic perturbation.

The fast ions distribution is represented as the sum of an analytical initial distribution, f_0, and an ensemble of marker particles which represent the change , δf. This separation of the fast ions distribution function is called the δf method.

In order to reduce the number of particles that need to be followed, each particle is uniformly weighted to represent several particles. These weighted particles, named "markers", follow the same dynamic as the real particles and enable the representation of more particles than are actually followed.

4.1 Coordinate System

The straight field line coordinates chosen in HAGIS [3] takes the poloidal flux ψ_p as the radial coordinate, the angle θ as the poloidal angle coordinate and deforms the toroidal angle coordinate ζ to obtain straight field lines (fig.4). Due to this deformation, the coordinates are no longer orthogonal and their Jacobian is no longer unitary. The Jacobian is given by :

$$\mathcal{J} = \frac{I + gq}{B^2}$$

where I is the toroidal current, g the poloidal current, q the safety factor and B the magnetic field.

In order to carry out integrals of the distribution function over velocity and space, it is necessary to correctly express the corresponding physical phase-space volume element.

$$d\Gamma^{(p)} = d^3v d^3x = \underbrace{2\pi v^2 dv d\lambda}_{\text{velocity element}} \underbrace{\mathcal{J} d\psi_p d\theta d\zeta}_{\text{spatial element}}$$

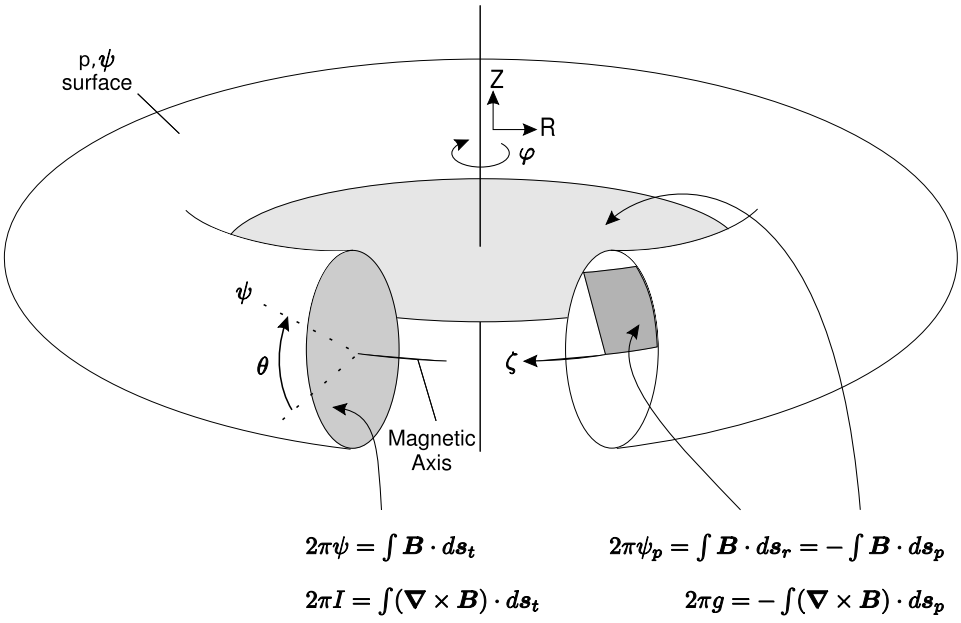

Figure 4 – Overview of the HAGIS coordinates (figure from [3])

where $\lambda = v_\parallel/v$ is the pitch angle and the $2\pi v^2$ term arises from the conservation of the magnetic moment $\mu = mv_\perp^2/2B$.

HAGIS solves the canonical equations of Hamilton to follow the fast ion guiding centres. The canonical variables used are the three coordinates θ, ζ and the gyro-phase ξ and the three corresponding canonical momenta, given by

$$P_\theta = \rho_\parallel I + \psi + \tilde{A}_\theta \quad (14)$$

$$P_\zeta = \rho_\parallel g + \psi_p + \tilde{A}_\zeta \quad (15)$$

$$P_\xi = \mu \quad (16)$$

where $\rho_\parallel = v_\parallel/\omega_{ci}$ and $\tilde{\boldsymbol{A}}$ is the electromagnetic vector potential representing the perturbation.

Hence, the canonical phase-space element is written as

$$d\Gamma^{(c)} = d\xi dP_\xi d\theta dP_\theta d\zeta dP_\zeta = 2\pi d\mu d\theta dP_\theta d\zeta dP_\zeta$$

where the integration over $d\xi$ also comes from the magnetic moment's conservation.

Finally, the Hamiltonian is given by

$$\mathcal{H} = \frac{1}{2}mv_{\parallel}^2 + \mu B + e\Phi$$

where Φ is the electric potential representing the perturbation.

4.2 Representation of the Fast Particles Distribution

In HAGIS , the initial fast particles distribution, f_0 may be specified in terms of the unperturbed constants of the motion : the energy $\mathcal{E}$, the canonical toroidal angular momentum P_ζ and the magnetic moment μ. To specify the initial particles distribution in terms of these conserved quantities ensure that the initial fast particles distribution will remain constant in the HAGIS coordinates system. This allow to efficiently separate the distribution function into a constant initial function f_0 and a function δf representing only the changes.

However, it isn't very convenient to specify the f_0 function in terms of the canonical momentum P_ζ. It is more natural to specify it in terms of the radial flux function. But, specifying the distribution function through the poloidal flux ψ_p would lead to a function that is not constant in time. So, in order to keep the conservation of the distribution function, HAGIS uses an average of the poloidal flux, $\langle\psi_p\rangle$, based on the definition of P_ζ (eq. 15), which is defined as a function of the constants of the motion.

$$\langle\psi_p\rangle = \begin{cases} R_0\sqrt{\frac{2}{m}(\mathcal{E}-\mu B_0)} - P_\zeta^{(0)}, & \text{for } \mathcal{E} > \mu B_0 \quad \text{(Co-passing)} \\ -P_\zeta^{(0)}, & \text{for } \mathcal{E} < \mu B_0 \quad \text{(Trapped)} \\ -R_0\sqrt{\frac{2}{m}(\mathcal{E}-\mu B_0)} - P_\zeta^{(0)}. & \text{for } \mathcal{E} > \mu B_0 \quad \text{(Counter-passing)} \end{cases} \tag{17}$$

This reduces the statistical noise in the calculation arising from the use of a finite number of simulation marker particles without quantitatively affecting the result.

5 Simulation

5.1 Equilibrium

The equilibrium has been created with the code EFIT++ which solves the Grad-Shafranov equation of force balance using experimental data. In our case, the experimental constraints were the external magnetic and the kinetic measurements (fig. 5). The equilibrium has then been converted to a straight field line equilibrium with the HELENA code to be ready to be used in HAGIS (fig. 6 and 7).

Equilibrium	
Radial position of the magnetic axis, R_{mag}	0.94 m
Vertical position of the magnetic axis, z_{mag}	-0.25 m
Magnetic field on axis, B_{mag}	0.53 T
Safety factor on axis, q_0	0.98
ψ_p at the edge, ψ_{edge}	7.153 $\times 10^{-2}$ m^2T

Table 2 – Equilibrium's parameters

5.2 Perturbations

HAGIS allows to specify the perturbation either analytically or from a linear MHD stability code such as MISHKA. The perturbation has been specified analytically, based on the results of MISHKA, to simplify scans in the parameters.

The eigenfunction used to represent the $m = 1$, $n = 1$ internal kink is given by

$$\phi_s(s) = \frac{s}{e^{(s-s(q=1))/\Delta s(q=1)} + 1} ,$$

where $s = \sqrt{\hat{\psi}_p} = \sqrt{\frac{\psi_p}{\psi_{p,edge}}}$ is the normalised radial coordinate used in HAGIS , $s(q = 1)$ is the position of the $q = 1$ surface and $\Delta s(q = 1)$ represents the width of the step at the $q = 1$ surface (fig. 9).

The amplitude of the perturbation is varied during each burst according to the following evolution

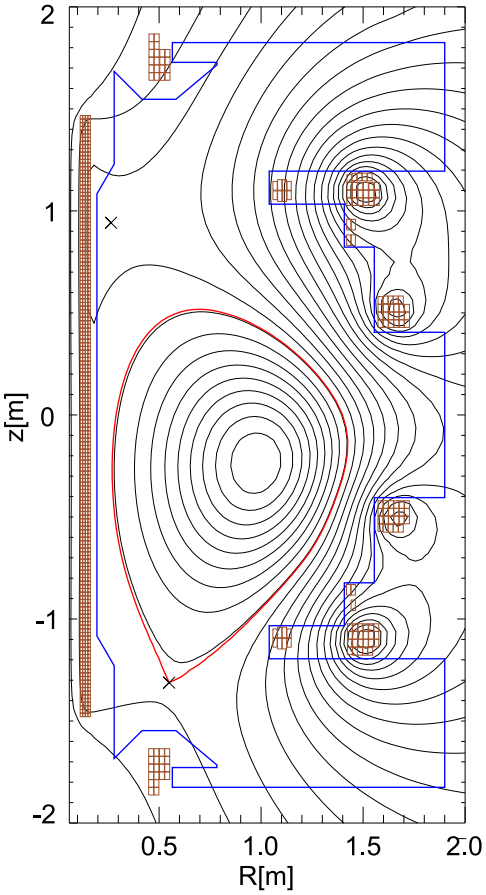

Figure 5 – EFIT++ reconstruction of the MAST 18808 shot equilibrium at 282ms showing the single null divertor down-shifted plasma.

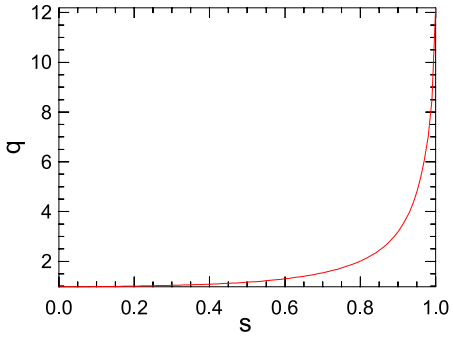

Figure 6 – Safety factor profile.

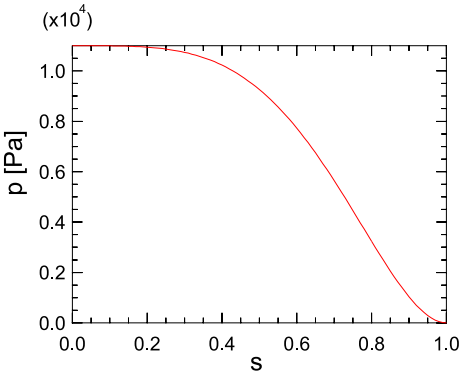

Figure 7 – Pressure profile.

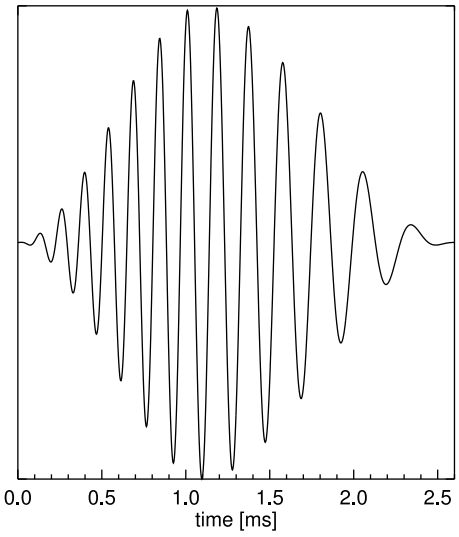

Figure 8 – Amplitude evolution of the perturbation.

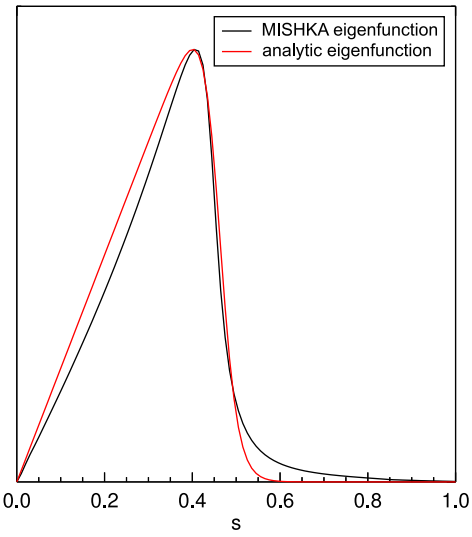

Figure 9 – Radial variation of the n=1, m=1, harmonic of the eigenfunction.

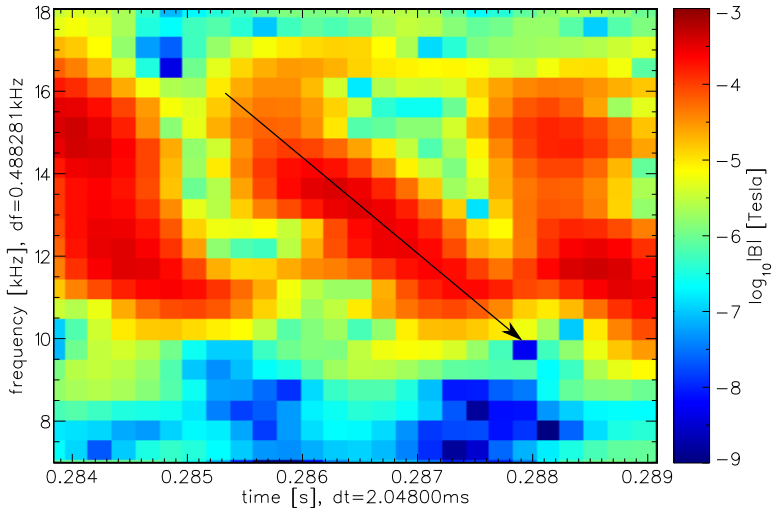

Figure 10 – RMS values of the Mirnov coil's signal for shot 18808 at 285ms. The arrow represents the analytic frequency evolution used.

$$A_{norm}(t) = \begin{cases} \frac{(3t_{sat}-2t)t^2}{t_{sat}^3} , & \text{for } t < t_{sat} \quad \text{(Growing)} \\ \frac{(3(t_{period}-t_{sat})-2(t_{period}-t))(t_{period}-t)^2}{(t_{period}-t_{sat})^3} , & \text{for } t \geq t_{sat} \quad \text{(Decaying)} \end{cases}$$

where t_{period} is the period of the bursts and t_{sat} is the time when the amplitude reaches its maximum within each period.

Its frequency is swept at a constant rate to match the observed data (fig. 10) taking into account a plasma rotation of 8 kHz (fig. 8 and 1) , giving a time evolution as

$$\phi_t(t) = A_{norm}(t)e^{-i(\omega_0 t + \frac{1}{2}\omega_{sweep}t^2)} ,$$

where ω_0 is the initial frequency and ω_{sweep} is the sweeping rate. The frequency is therefore given by

$$\omega_0 + \omega_{sweep}t .$$

A rough estimate of the perturbation's amplitude is given by the soft X-rays data. One can see that the perturbation is oscillating between two soft X-ray channels of the horizontal camera. Given that the distance between

two lines of sight at the magnetic axis is $\sim 5\,\mathrm{cm}$ (33 lines of sight spread over $\sim 1.6\,\mathrm{m}$) and that the plasma diameter, d, is about 1.5 m, an upper limit for the magnetic amplitude of the perturbation is roughly $\delta B/B \sim \xi/d \sim 0.01$.

The different parameters used for this experiment are given in table 3.

Perturbation	
Position of the $q = 1$ surface, $s(q = 1)$	0.46
Width of the step at the $q = 1$ surface, $\Delta s(q = 1)$	0.02
Time of saturation, t_{sat}	1.1 ms
Period of the bursts, t_{period}	2.6 ms
Initial frequency in plasma frame, ω_0	8 kHz
Sweeping rate, ω_{sweep}	-2.11 MHz/s
Upper limit of the amplitude, $\delta B/B$,	0.01

Table 3 – Perturbation's parameters

5.3 Fast Ion Distribution

The initial fast ion distribution f_0 has been derived from a TRANSP analysis. It has been assumed that the distribution was an isotropic separable function of energy and radial position. Attempts to interpolate the fast ions' distribution function from TRANSP were made. However, the data was too noisy and the use of an analytic description was held to be the best. Details of the raw TRANSP data are given in Appendix A.

The energetic distribution is a slowing down distribution resulting from neutral beam injection and is given by [12]

$$f_{0,E}(E) = \frac{1}{E^{3/2} + E_c^{3/2}} \mathrm{Erf}_c \left(\frac{E - E_0}{\Delta E} \right) \ ,$$

where the parameters E_c, E_0 and ΔE have been fitted from the TRANSP data (fig. 11) and are given in table 4.

The radial distribution of fast ion resulting from off-axis NBI heating has been represented by the sum of three Gaussians.

$$f_{0,s}(s) = e^{-(\frac{s-s_0}{\Delta s_0})^2} + e^{-(\frac{s+s_0}{\Delta s_0})^2} + R \cdot e^{-(\frac{s}{\Delta s_1})^2} \ ,$$

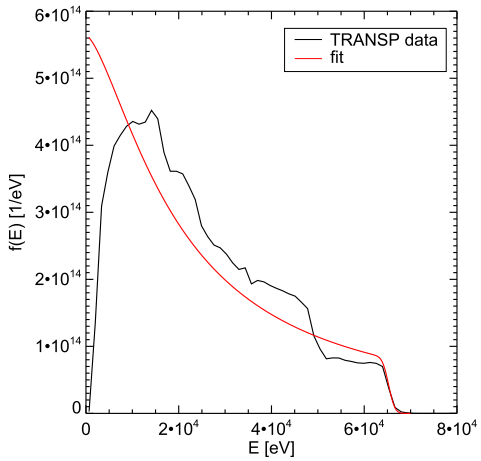

Figure 11 – Fit of the fast ions's energetic distribution from TRANSP

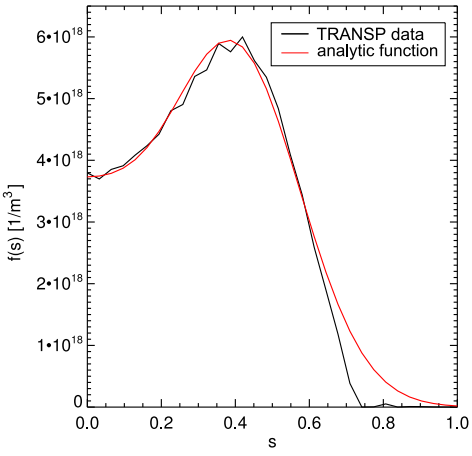

Figure 12 – The TRANSP radial distribution and the analytic distribution used in HAGIS

where the parameters, s_0, Δs_0, Δs_1 are expressed in terms of the HAGIS coordinate s and are given in table 4.

Two symmetrically opposed Gaussians represent the off-axis contribution and a centered one represents the on-axis contribution. The use of symmetric distribution ensure that the distribution is flat in its centre.

The initial fast ions' distribution function is finally given by

$$f_0(E, s) = C \cdot f_{0,E}(E) \cdot f_{0,s}(s) \ ,$$

where C is a constant adjusted to ensure that integration over the whole phase space matches the total number of fast ions given by TRANSP ($\sim 1.5 \times 10^{19}$).

5.4 Calculation of the Diffusion Coefficient

The diffusion coefficient is calculated from Fick's law

$$\boldsymbol{\Gamma}(\boldsymbol{x}, t) = -D \boldsymbol{\nabla} n(\boldsymbol{x}, t) \ , \tag{18}$$

where $\boldsymbol{\Gamma}(\boldsymbol{x}, t) = n\boldsymbol{v}$ is the particles flux and n is the density of particles. In HAGIS coordinates ($\xi^2 \equiv \psi_p, \xi^2 \equiv \theta, \xi^3 \equiv \zeta$), the velocity $\boldsymbol{v}$ is expressed as

Fast ions distribution	
Energetic distribution	
Injection energy, E_0	65.3 keV
Width of the injection peak, ΔE	1.49 keV
Slowing down parameter, E_c	20.0 keV
Radial distribution	
Injection tangency radius, s_0	0.4
Width of the injection peak, Δs_0	0.25
Ratio of on-axis versus off-axis density, R	0.5
Width of the on-axis peak, Δs_1	0.25

Table 4 – Fast ions distribution's parameters

$$\boldsymbol{v} = \frac{d\boldsymbol{x}}{dt} = \frac{\partial \boldsymbol{x}}{\partial \psi_p}\frac{d\psi_p}{dt} + \frac{\partial \boldsymbol{x}}{\partial \theta}\frac{d\theta}{dt} + \frac{\partial \boldsymbol{x}}{\partial \zeta}\frac{d\zeta}{dt} = \frac{\partial \boldsymbol{x}}{\partial \psi_p}v^{\psi_p} + \frac{\partial \boldsymbol{x}}{\partial \theta}v^{\theta} + \frac{\partial \boldsymbol{x}}{\partial \zeta}v^{\zeta} \ ,$$

where $\frac{\partial \boldsymbol{x}}{\partial \xi^i}$ is the i^{th} contravariant basis vector. The covariant radial velocity is then given by

$$v_{\psi_p} = \boldsymbol{v}\cdot\frac{\partial \boldsymbol{x}}{\partial \psi_p} = \frac{\partial \boldsymbol{x}}{\partial \psi_p}\frac{\partial \boldsymbol{x}}{\partial \xi^i}v^i = \mathrm{g}_{\psi_p i}v^i \cong \mathrm{g}_{\psi_p\psi_p}v^{\psi_p} = \mathrm{g}_{\psi_p\psi_p}\dot{\psi} \ ,$$

with $\mathrm{g}_{\psi_p\zeta} \equiv 0$ and $\mathrm{g}_{\psi_p\theta} \equiv 0$ for an orthogonal system, where $\mathrm{g}_{ij} = \frac{\partial \boldsymbol{x}}{\partial \xi^i}\frac{\partial \boldsymbol{x}}{\partial \xi^j}$ is the HAGIS covariant metric tensor.

Fick's law in the radial direction can be written

$$\Gamma_{\psi_p}(\psi_p, t) = nv_{\psi_p} = -D_r\frac{\partial n(\psi_p, t)}{\partial \psi_p} \ .$$

The radial diffusion coefficient is therefore given by

$$D_r = -\frac{\Gamma_{\psi_p}}{\partial n/\partial \psi_p} = -\frac{n\dot{\psi}_p\,\mathrm{g}_{\psi_p\psi_p}}{\partial n/\partial \psi_p} \ . \tag{19}$$

To calculate the value of the density and the particle flux at the radial position ψ_p, we used the average value over a small volume ΔV between two flux surfaces located at ψ_p and $\psi_p + \Delta\psi_p$.

The density is given by

$$\begin{aligned}
\langle n(\psi_p,t)\rangle &= n_0(\psi_p)+\delta n(\psi_p,t)\\
&= \frac{\int_{\Delta V} dx^3 \int dv^3 f_0}{\int_{\Delta V} dx^3} + \frac{\int_{\Delta V} dx^3 \int dv^3 \delta f}{\int_{\Delta V} dx^3}\\
&= \frac{\int_{\Delta V} \mathcal{J} d\psi_p d\theta d\zeta \int 2\pi v^2 dv d\lambda f_0}{\int_{\Delta V} \mathcal{J} d\psi_p d\theta d\zeta} + \frac{\int_{\Delta V} \mathcal{J} d\psi_p d\theta d\zeta \int 2\pi v^2 dv d\lambda \delta f}{\int_{\Delta V} \mathcal{J} d\psi_p d\theta d\zeta}\\
&= \frac{\int_{\Delta V} f_0 d\Gamma^{(p)}}{\Delta V} + \frac{\sum_i \delta f_i \Delta\Gamma_i^{(p)}}{\Delta V}\ . \qquad (20)
\end{aligned}$$

where the index i labels quantities associated to the simulation markers particles within the volume ΔV.

Similarly, the radial flux is calculated as

$$\begin{aligned}
\langle \Gamma_{\psi_p}(\psi_p,t)\rangle &= \langle \Gamma_{\psi_p,0}(\psi_p)+\delta\Gamma_{\psi_p}(\psi_p,t)\rangle\\
&= \frac{\int_{\Delta V} \mathcal{J} d\psi_p d\theta d\zeta \int 2\pi v^2 dv d\lambda \delta f \dot{\psi_p}\, \mathrm{g}_{\psi_p\psi_p}}{\int_{\Delta V} \mathcal{J} d\psi_p d\theta d\zeta}\\
&= \frac{\sum_i \delta f_i \dot{\psi_p}_i\, \mathrm{g}_{\psi_p\psi_p,i} \Delta\Gamma_i^{(p)}}{\Delta V}\ , \qquad (21)
\end{aligned}$$

because the initial radial flux, $\Gamma_{\psi_p,0}(\psi_p)$, is equal to zero.

In those two expressions (eq. 20 and 21) the value of ψ_p is taken as the value calculated from the equilibrium constant of the motion (eq. 17). With full ψ_p, n_0 was noisier. And, therefore, $\dot{\psi_p}$ is calculated as

$$\langle\dot{\psi_p}\rangle = \begin{cases} R_0 \frac{\dot{\mathcal{E}}}{\sqrt{2m(\mathcal{E}-\mu B_0)}} - \dot{P}_\zeta, & \text{for } \mathcal{E} > \mu B_0 \quad \text{(Co-passing)}\\ -\dot{P}_\zeta, & \text{for } \mathcal{E} < \mu B_0 \quad \text{(Trapped)}\\ -R_0 \frac{\dot{\mathcal{E}}}{\sqrt{2m(\mathcal{E}-\mu B_0)}} - \dot{P}_\zeta, & \text{for } \mathcal{E} > \mu B_0 \quad \text{(Counter-passing)} \end{cases} \qquad (22)$$

5.5 Numerical Parameters

The simulations were performed on 16 Pentium IV Xenon processors running at 3.06 GHz in a typical run time of one hour per run. The numerical parameters used are shown in table 5.

Numerical Parameters	
Integrator tolerance, $\delta\mathcal{E}/\mathcal{E}$	1×10^{-6}
Initial step size	1×10^{-8} s
Simulated time,	2.6×10^{-3} s
Number of markers,	1,050,000

Table 5 – Numerical parameters

6 Results

Computational simulations were performed to simulate the fast ions diffusion coefficient arising in MAST shot 18808 at 285 ms as a results of fishbone bursts. Results obtained with the parameters given in section 5 are displayed in the following section.

6.1 Simulation of MAST Shot 18808

The effect of a diffusive type of transport is illustrated in figure 13 where the fast ions' radial distribution is broadened by the diffusion. The change in the density profile due to only one fishbone being small compared to the equilibrium density, we show (fig. 14) the change in the density profile, δn, rather than the the evolution of the full density profile.

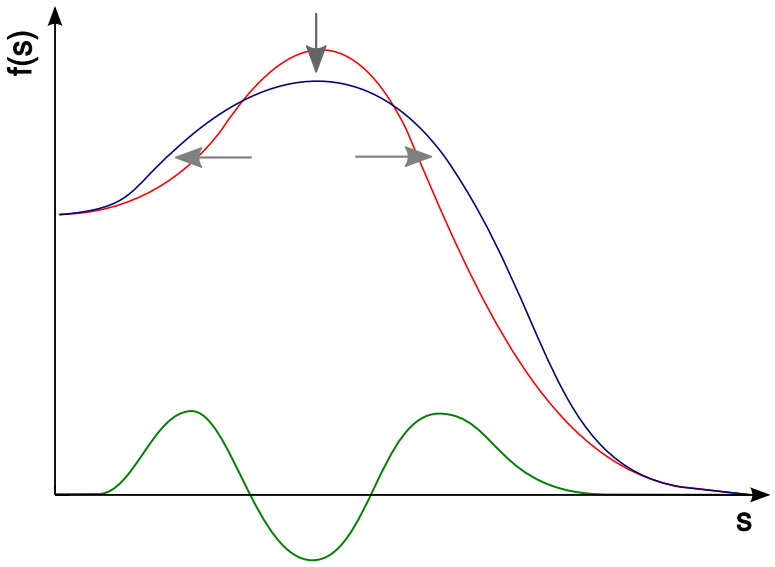

Figure 13 – Illustration of the broadening of the radial fast ions distribution due to fast ion diffusion. The red line shows the initial distribution, the blue one shows the distribution after the fast ions redistribution and the green line shows the change in the distribution.

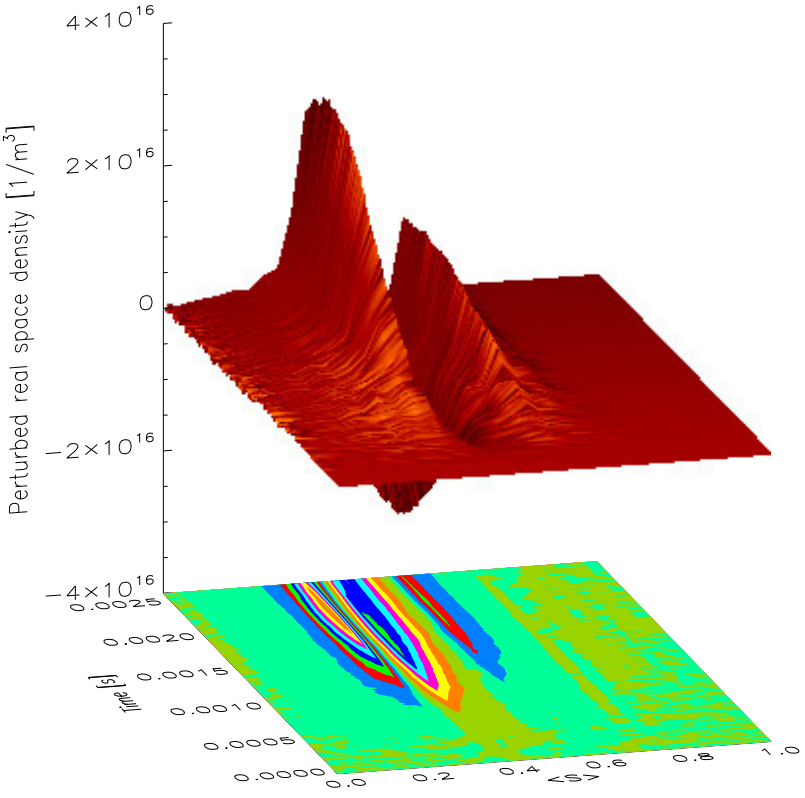

Figure 14 – Change in fast ion radial density profile with time for a perturbation amplitude of $\delta B/B = 1 \times 10^{-4}$

Figure 14 shows the radial evolution of the change in the fast ion density, $\delta n(s,t)$. It shows the broadening of the fast ion radial distribution as the density reduces where the initial distribution has its peak value (at $s = 0.4$, fig. 12) and increases on either side. The density evolution follows the fishbone growing and the change persists when the fishbone decays away completely.

As the ensemble of the simulation markers is evolved, the radial flux arising from their interaction with the fishbone perturbation is calculated in accordance with equation 21 and shown in figure 15.

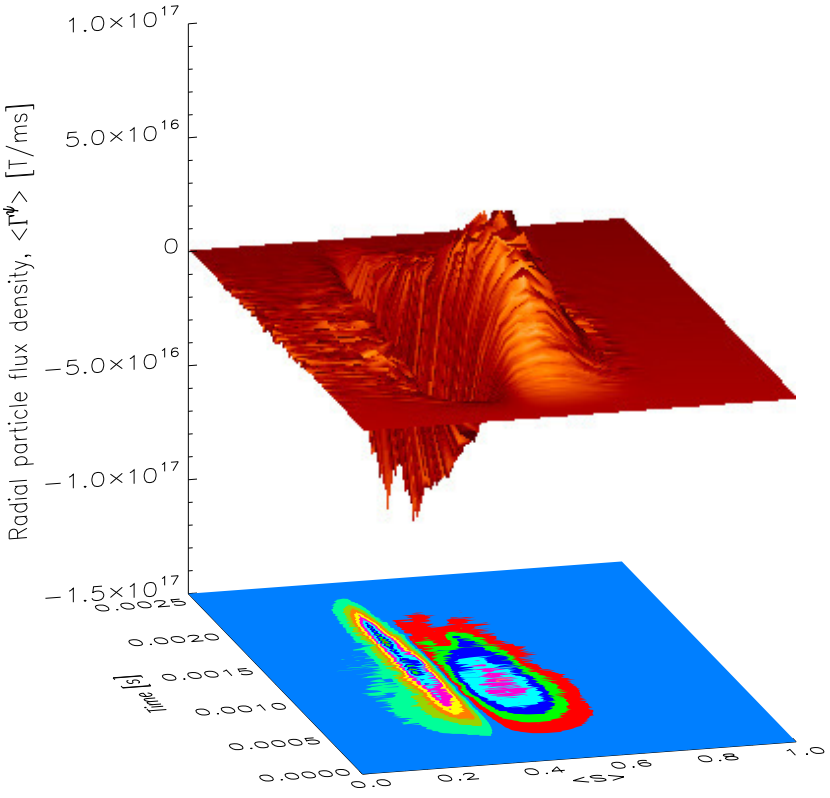

Figure 15 – Evolution of the radial fast ions flux profile for a perturbation amplitude of $\delta B/B = 1 \times 10^{-4}$

Figure 15 shows the evolution of the fast ions radial flux. It is negative where the fast ions are moved inward and positive where they are moved outward. It clearly indicates that the radial distribution is broadened by the interaction with the fishbone as explained in figure 13. The flux increases as the fishbone grows and then decreases with it until the next fishbone.

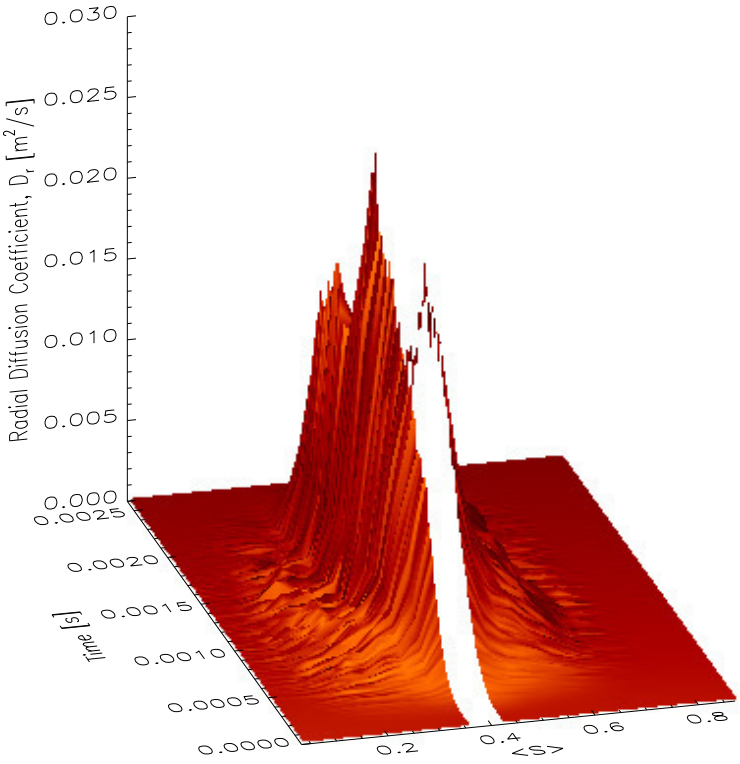

Figure 16 – Evolution of the radial diffusion coefficient's profile for a perturbation amplitude of $\delta B/B = 1 \times 10^{-4}$

The value of the diffusion coefficient for this simulation is given in figure 16. The values at $s = 0.4$ were removed because they correspond to the point where the density profile is flat (fig. 12) and, therefore, its derivative equal to zero. As the diffusion coefficient is calculated by dividing the particles flux by the radial derivative of the density (eq. 19), these values are not defined.

The amplitude of the perturbation used in this simulation was 1×10^{-4} and the diffusion coefficient is about one order of magnitude smaller that the one expected. With an amplitude of 7×10^{-4} the peak values of the diffusion coefficient reach the expected values (fig 17). As the statistical noise increases with the perturbation amplitude, a boxcar average over 3 radial points ($\sim$ 4 cm) and 5 time points (0.05 ms) has been performed. This

smoothing fills the removed values at $s = 0.4$ with a linear interpolation from both sides of the gap.

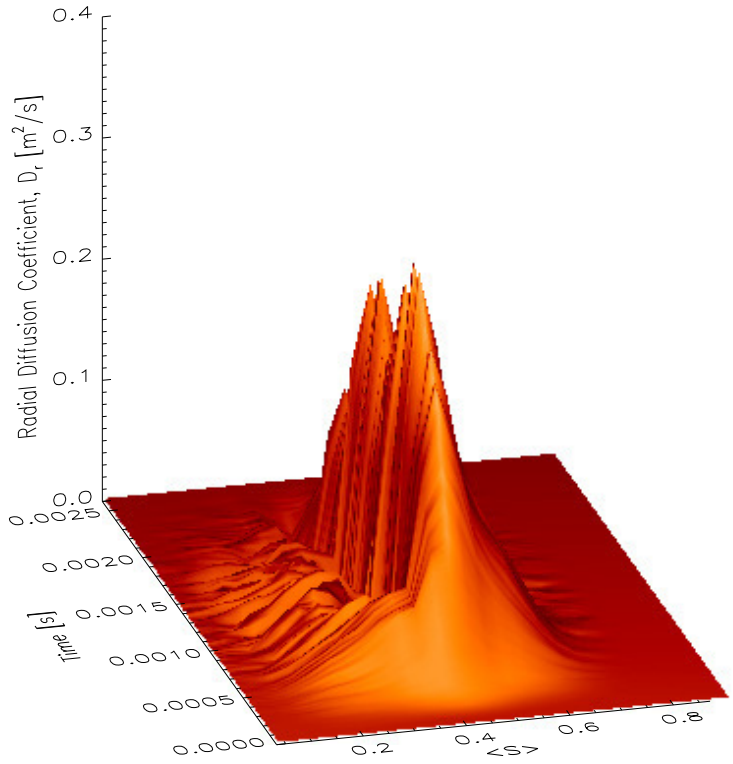

Figure 17 – Evolution of the boxcar averaged diffusion coefficient's radial profile for a perturbation amplitude of $\delta B/B = 7 \times 10^{-4}$.

This initial simulation has a diffusion coefficient comparable with that required to explain the experimental observations [1]. The robustness of the result to plausible change in the physical simulation is investigated in the next sections.

6.2 Varying Simulation's Parameters

The diffusion coefficient profile has a singularity at $s = 0.4$ where the density gradient is equal to zero. It is therefore important to choose representing values that are not at the position of the singularity. The values used for comparison were chosen where the density profile is the steepest, i.e. on both sides of the density peak at $s = 0.19$ and $s = 0.55$. Taking the maximum value of D_r at these positions gives a diffusion coefficient for the outward transport, $D_{r,out}$, and a diffusion coefficient for the inward transport, $D_{r,in}$.

6.2.1 Variation of Diffusion Coefficient with Amplitude

Simulations were carried out with different perturbation amplitudes in order to investigate the dependence of the diffusion coefficient on the latter.

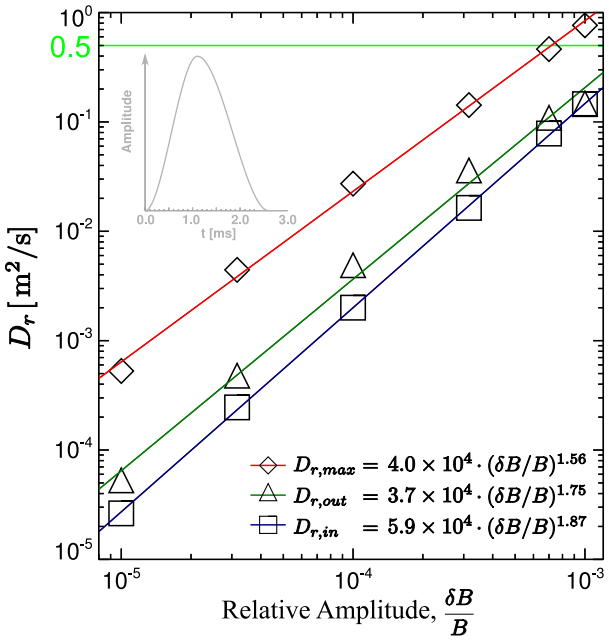

Figure 18 – Outward transport diffusion coefficient, inward diffusion coefficient and maximum value of the diffusion coefficient for different peak amplitudes of the fishbone oscillation. The horizontal green line shows the value of the experimental diffusion coefficient

Figure 18 shows that the values of the diffusion coefficient scale with

the amplitude with an exponent α comprised between 1.56 and 1.87. This shows the process is nonlinear, as expected, since, as the mode's amplitude increases by keeping the same period length, the growth rate also increases as it now has to grow to a bigger amplitude within the same time period.

6.2.2 Effect of Mode Frequency Range upon Diffusion Coefficient

Changing the frequency over which the mode sweeps in the plasma frame (i.e. corrected for plasma rotation as compared with the lab frame) may be expected to change the region of particles in velocity space that are influenced by the fishbones.

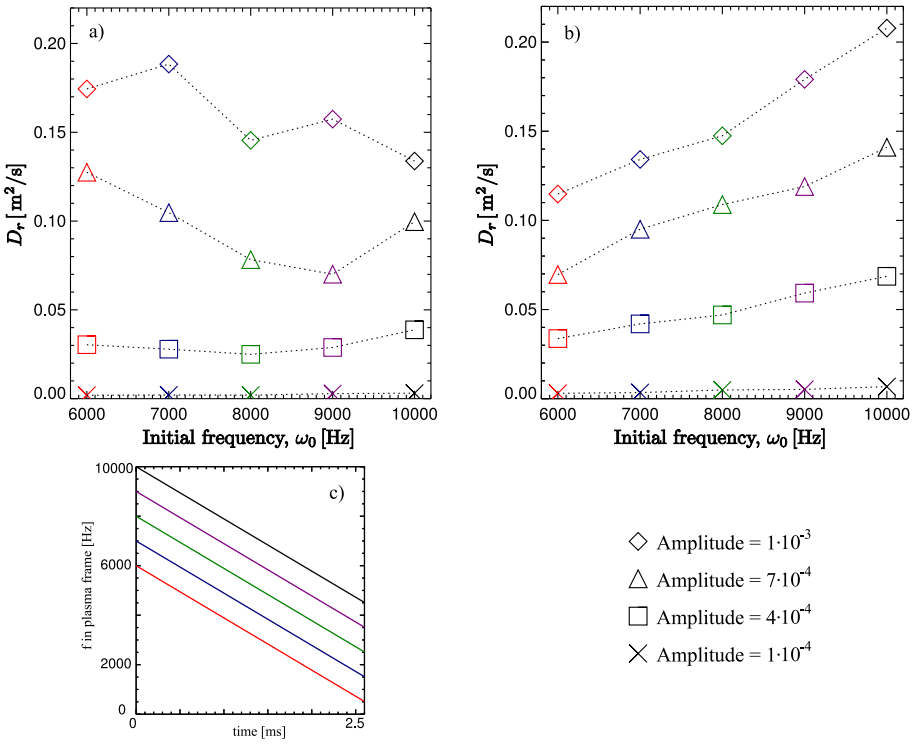

Figure 19 – Values of the diffusion coefficient for different initial frequencies and amplitudes of the perturbation. a) shows the D_r values for the inward transport, b) shows the values for outward transport and c) shows the corresponding frequency evolutions. The values corresponding to the experimental parameter are shown in green.

Figure 19 shows the variation in the value of the inward and outward diffusion coefficients for different mode frequency ranges at different mode amplitudes. The dependence of the diffusion coefficient on the initial frequency is found to be weak. The outward coefficient slightly increases as the initial frequency increases and the inward coefficient doesn't vary much. The difference between the inward and outward diffusion coefficient may be explained by the fact that the perturbation doesn't interact with particles that have the same type of orbits.

6.2.3 Effect of Frequency Sweeping Rate upon Diffusion Coefficient

The effect of the frequency sweeping rate upon the diffusion coefficient was also investigated since this will change the wave-particle power transfer. Particles interacting with the perturbation in a certain frequency range will feel the perturbation during a time that depends on the frequency sweeping rate. Changing the sweeping rate also changes the frequency at which the mode amplitude reaches its maximum.

The dependence of the diffusion coefficient on the sweeping rate is shown in figure 20. It is found that only a weak (nonlinear) dependence exits, independently of the amplitude.

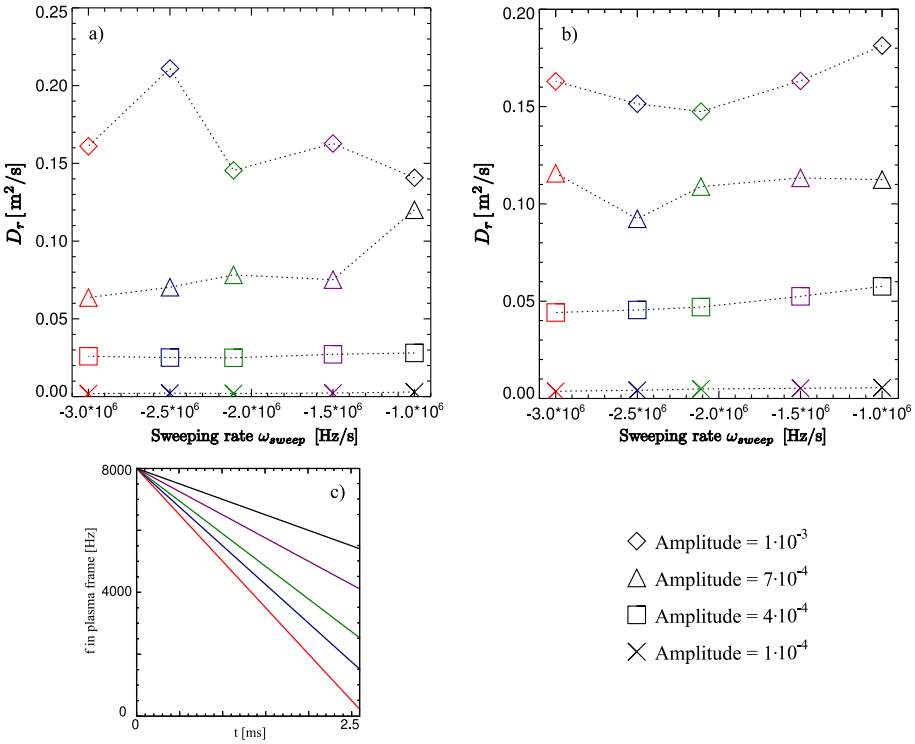

Figure 20 – Values of the diffusion coefficient for different sweeping rates of the perturbation's frequency and different mode's amplitudes. a) shows the D_r values for the inward transport, b) shows the values for outward transport and c) shows the corresponding frequency evolutions. The values corresponding to the experimental parameter are shown in green.

6.2.4 Effect of Saturation Time upon Diffusion Coefficient

Varying the saturation time of the mode changes the mode's growth rate and the frequency at which the mode amplitude has its maximum.

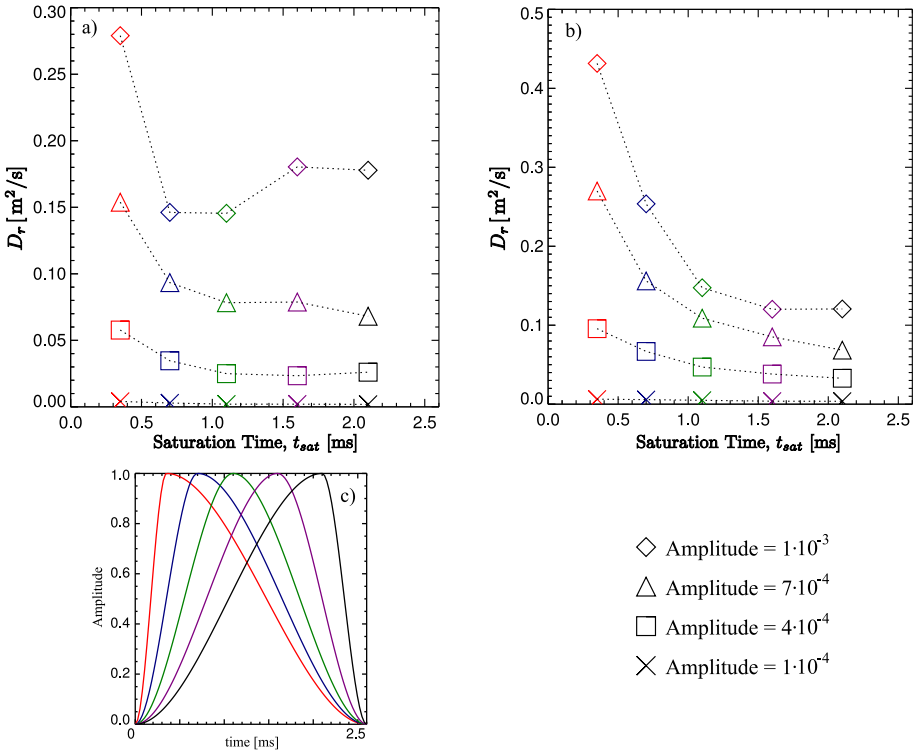

Figure 21 – Values of the diffusion coefficient for different saturation times and amplitudes of the perturbation. a) shows the D_r values for the inward transport, b) shows the values for outward transport and c) shows the corresponding mode evolutions. The values corresponding to the experimental parameter are shown in green.

Values of the diffusion coefficient for different saturation times and mode's amplitudes are shown in figure 21. It is found to be bigger when the saturation time is smaller, but the values stay in the range of the exprimental value.

6.2.5 Effect of Step's Width of the Eigenfunction upon Diffusion Coefficient

The description of the fishbone eigenfunction used in the simulations is an analytical approximation of the ideal MHD calculation. The inclusion of non-ideal effects may change the eigenfunction and thus the effect of different shapes of the eigenfunction has been investigated.

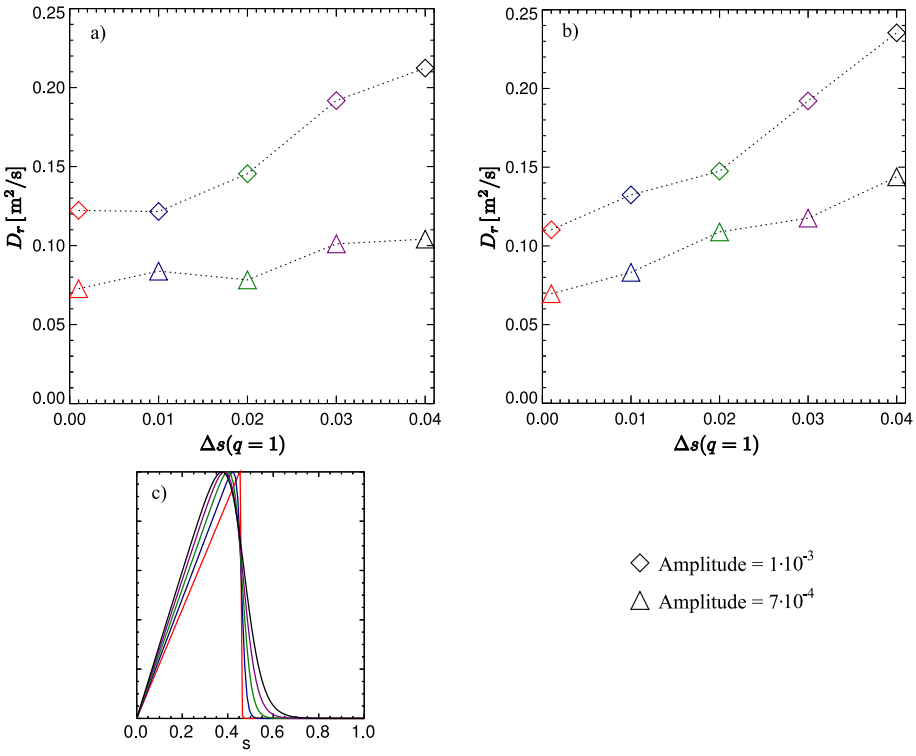

Figure 22 – Values of the diffusion coefficient for different width of the eigenfunction's step and different mode amplitudes. a) shows the D_r values for the inward transport, b) shows the values for outward transport and c) shows the corresponding eigenfunction. The values corresponding to the experimental parameter are shown in green.

Values of the diffusion coefficient for different step's width of the eigenfunction and mode's amplitudes are shown in figure 22. The diffusion coefficient weakly increase with the step's width of the eigenfunction.

7 Conclusion

In this Master's Thesis, simulations have been performed to quantify the amount of fast ions diffusion that arises from fishbone oscillations in MAST.

This work was motivated by the need to understand the deficit in the neutron rate that arose in TRANSP simulations of the MAST shot 18808. These simulations showed that only by invoking a fast ion radial diffusion coefficient of $D_r \sim 0.5$ m^2/s could the anomaly be explained.

The work presented here shows that a fast ion diffusion coefficient of 0.5 m^2/s can be explained by the radial redistribution of fast ions by $n = 1$, $m = 1$ fishbone oscillations. This assumption has been shown to be robust to variations of the fishbone's mode structure and temporal evolution (initial frequency, sweeping rate, saturation time and amplitude) where little variation in D_r were observed, the strongest dependence being with the mode amplitude.

Appendix

A Determination of Fast Ion Distribution Function

Since the 6-D distribution of fast ions present in a neutral beam heated MAST plasma is not directly measured, numerical simulations must be undertaken to determine it. These simulations have to take into account the source of fast ions from the neutral beam heating system, together with their transport and potential loss from the plasma edge.

TRANSP is a transport analysis code which does time and space-dependent analysis of current diffusion, energy and particle transport [13, 14]. It uses, whenever possible, experimental data to calculate local transport coefficients and features a sophisticated Monte Carlo beam treatment code, NUBEAM [2], which permits to calculate the fast ions distribution due to neutral beam injection.

The TRANSP fast ion distribution is given as a function of energy, pitch angle ($\lambda = v_{\|}/v$) and position. The position is expressed as an index following the flux surfaces. We tried to interpolate this function in this both HAGIS coordinates $(\mathcal{E}, P_\zeta, \mu)$, where it is irregularly gridded, and in the real space coordinates $(\mathcal{E}, R, Z, \mu)$, but our attempts were unsuccessful due to the scattered state of the data and the complexity of three and four dimensional interpolation of irregular data. We also tried to fit multidimensional functions but again the data wasn't smooth enough to get satisfying results.

It is only by intergrating over some dimensions and looking to one dimension at a time that it has been possible to suitably fit functions. We therefore decided to treat the distribution as a separable function of its variables.

Slices of the TRANSP data are shown in figure 23 showing the scattered state of the data. The distribution integrated over every energy and pitch angle values is shown in figure 24.

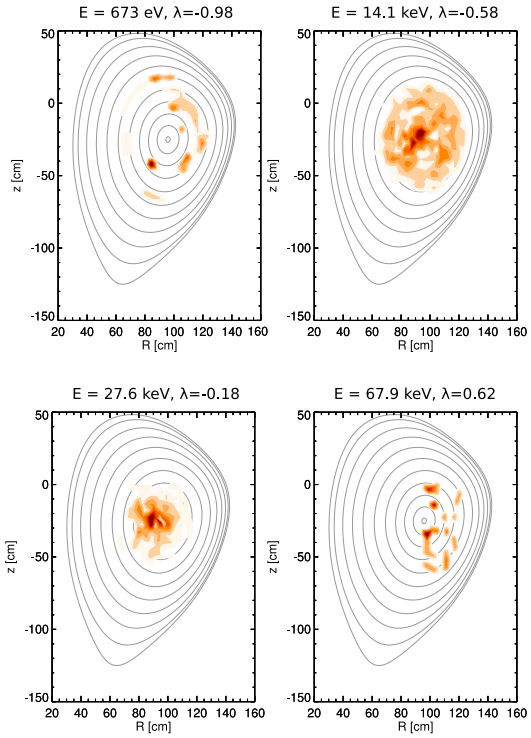

Figure 23 – Slices of the TRANSP fast ions distribution for different energies and pitch angles showing the scattered state of the data.

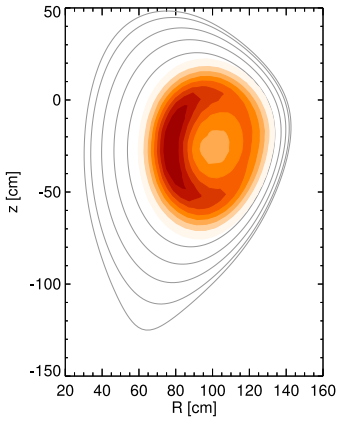

Figure 24 – TRANSP fast ion distribution integrated over energy and pitch angle.

References

[1] Turnyanskiy, M., Keeling, D. L., and Akers, R. J., 22nd IAEA Fusion Energy Conference, Geneva (2008) EX/P6 26.

[2] Pankin, A., McCune, D., Andre, R., Bateman, G., and Kritz, A., Computer Physics Communications **159** (2004) 157.

[3] Pinches, S. D., *Nonlinear Interaction of Fast Particles with Alfvèn Waves in Tokamaks*, PhD thesis, University of Nottingham, 1996.

[4] Wesson, J., *Tokamaks*, Oxford University Press, third edition, 2004.

[5] Dendy, R., editor, *Plasma Physics : An Introductory Course*, Cambridge University Press, 1996.

[6] Bateman, G., *MHD Instabilities*, The MIT Press, 1978.

[7] Ödblom, A., Breizman, B. N., Sharapov, S. E., Hender, T. C., and Pastukhov, V. P., Phys. Plasmas **9** (2002) 155.

[8] Kolesnichenko, Y. I., Lutsenko, V. V., and Marchenko, V. S., Phys. Rev. Lett. **82** (1999) 3260.

[9] Coppi, B. and Porcelli, F., Phys. Rev. Lett. **57** (1986) 2272.

[10] Nabais, F. and Borba, D., Phys. Plasmas **12** (2005) 102509.

[11] Chen, L., Ehite, R. B., and Roosenbluth, M. N., Phys. Rev. Lett. **52** (1984) 1122.

[12] Gaffey, J. D., J. Plasma Physics **16** (1976) 149.

[13] Goldston, R. J., *Topics in Confinement Analysis of Tokamaks with Auxiliary Heating*, volume I, pp.165-186, Basic Physical Processes of Toroidal Fusion Plasmas (Proc. Course and Workshop Varenna, 1985), 1986.

[14] Hawryluk, R., *An Empirical Approach to Tokamak Transport*, volume I, p. 19, Proc. Course and Workshop 1979, Rep. EUR-FU-BRU/XII/476/80, CEC, Brussels, 1980.